Structural and electronic properties of epitaxial graphene on SiC(0001): a review of growth, characterization, transfer doping and hydrogen intercalation

C Riedl, C Coletti, U Starke

Structural and electronic properties of epitaxial graphene on SiC(0001): A review of growth, characterization, transfer doping and hydrogen intercalation

C. Riedl, C. Coletti and U. Starke

Max-Planck-Institut für Festkörperforschung, Heisenbergstr. 1, D-70569 Stuttgart

E-mail: u.starke@fkf.mpg.de

Abstract.

Graphene, a monoatomic layer of graphite hosts a two-dimensional electron gas system with large electron mobilities which makes it a prospective candidate for future carbon nanodevices. Grown epitaxially on silicon carbide (SiC) wafers, large area graphene samples appear feasible and integration in existing device technology can be envisioned. This article reviews the controlled growth of epitaxial graphene layers on SiC(0001) and the manipulation of their electronic structure. We show that epitaxial graphene on SiC grows on top of a carbon interface layer that – although it has a graphite-like atomic structure – does not display the linear π-bands typical for graphene due to a strong covalent bonding to the substrate. Only the second carbon layer on top of this interface acts like monolayer graphene. With a further carbon layer, a graphene bilayer system develops. During the growth of epitaxial graphene on SiC(0001) the number of graphene layers can be precisely controlled by monitoring the π-band structure. Experimental fingerprints for in-situ growth control could be established. However, due to the influence of the interface layer, epitaxial graphene on SiC(0001) is intrinsically n-doped and the layers have a long-range corrugation in their density of states. As a result, the Dirac point energy where the π-bands cross is shifted away from the Fermi energy, so that the ambipolar properties of graphene cannot be exploited. We demonstrate methods to compensate and eliminate this structural and electronic influence of the interface. We show that the band structure of epitaxial graphene on SiC(0001) can be precisely tailored by functionalizing the graphene surface with tetrafluoro-tetracyanoquinodimethane (F4-TCNQ) molecules. Charge neutrality can be achieved for mono- and bilayer graphene. On epitaxial bilayer graphene, where a band gap opens due to the asymmetric electric field across the layers imposed by the interface, the magnitude of this band gap can be increased up to more than double of its initial value. The hole doping allows the Fermi level to shift into the energy band gap. The impact of the interface layer can be completely eliminated by decoupling the graphene from the SiC substrate by a hydrogen intercalation technique. We demonstrate that hydrogen can migrate under the interface layer and passivate the underlying SiC substrate. The interface layer alone transforms into a quasi-free standing monolayer. Epitaxial monolayer graphene turns into a decoupled bilayer. In combination with atmospheric pressure graphitization, the intercalation process allows to produce quasi-free standing epitaxial graphene on large SiC wafers and represents a highly promising route towards epitaxial graphene based nanoelectronics.

1. Introduction

The unconventional two-dimensional electron gas properties of graphene have attracted tremendous interest in recent years for this material [1, 2, 3, 4, 5, 6]. With its outstanding electronic transport parameters it is in addition considered one of the most promising materials for future nano-scaled carbon electronics for developments beyond the Si CMOS era. A big surge of graphene research was initiated, when graphene flakes could be successfully isolated by micromechanical cleavage of graphite [7] and contemporaneously, graphene layers could be epitaxially grown on silicon carbide (SiC) samples [8]. Since then, graphene has also been grown on metals [9] and chemically synthesized [10], in particular by a chemical reduction of graphene oxide [11]. Graphene could even be produced completely free-standing by suspending the graphene flakes [12] or – as will be reviewed in this paper – quasi-free, by decoupling the epitaxial graphene layers from SiC by hydrogen intercalation [13]. Theoretically, graphene was predicted to be thermodynamically unstable as a free standing layer [14, 15]. However, the recent progress in graphene isolation should not be considered a contradiction to theory since the stability of the free graphene is given by crumpling or wrinkling [12], and the quasi-free standing layers are still van-der-Waals bound to the substrate [13].

Strictly, the notion graphene represents a single layer of graphite. However, the description "graphene" is not only used for single layers, but also for bilayer and few-layer graphene (up to about ten layers) which all can be viewed as different types of two dimensional crystals [4]. The carbon atoms in a graphene layer are sp^2-hybridized forming three in-plane σ-bonds per atom which in turn leads to the formation of a hexagonal planar layer with a honeycomb-like atomic arrangement. The hexagonal graphene lattice is displayed in a top view model in figure 1 (a) and exhibits a basis with two carbon atoms, A and B, per unit cell. These two atoms form two equivalent sublattices (depicted in green and red, respectively, in the figure). The corresponding

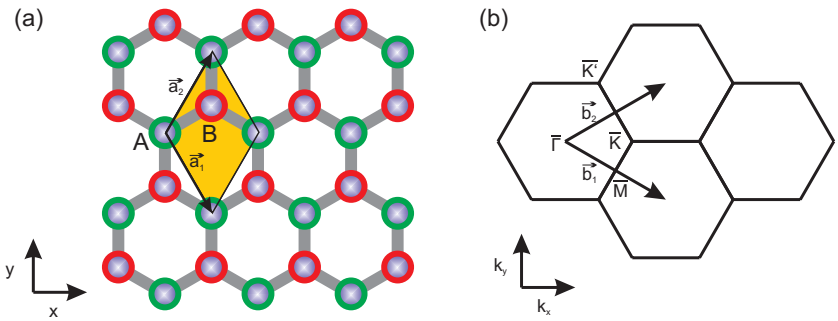

Figure 1. (a) Honeycomb lattice structure of graphene. Its unit cell (yellow) contains a basis of two atoms, which leads to two equivalent sublattices (A/green and B/red). The 2D-real space unit vectors $\vec{a}_1$ and $\vec{a}_2$ are indicated. (b) Graphene Brillouin zone in reciprocal space together with the reciprocal unit vectors, $\vec{b}_1$ and $\vec{b}_2$, and high symmetry points ($\overline{\Gamma}$, $\overline{M}$, $\overline{K}$ and $\overline{K}'$) indicated. The k_x/k_y coordinate system corresponds to the measurement orientation in ARPES described below.

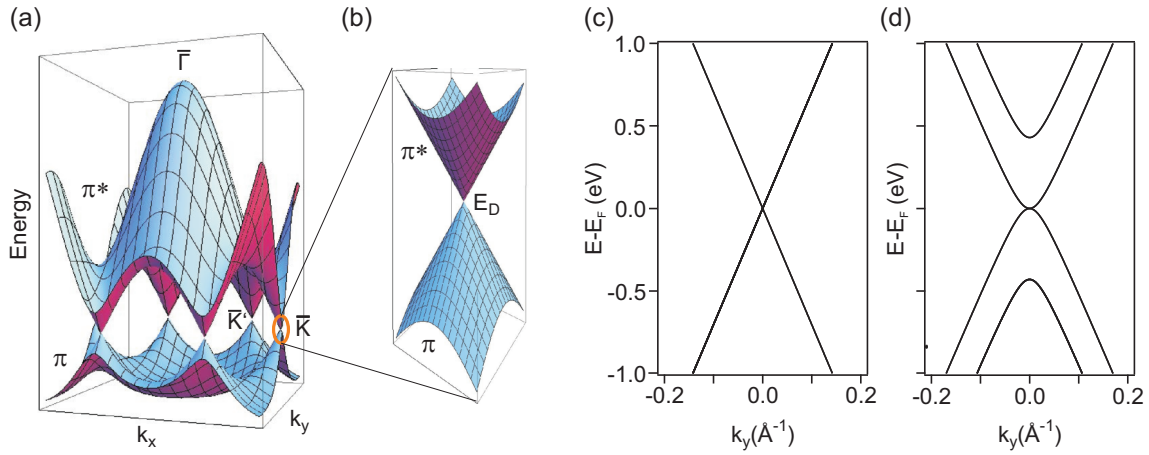

Figure 2. (a) The graphene π-band dispersion in three-dimensional representation as calculated from the original tight-binding approach by P.R. Wallace [1]. The nearest and next nearest-neighbor interaction parameters are set to $t = 2.7$ eV and $t' = 0.2\,t$, respectively [16, 17]. (b) Zoomed region close to the $\overline{\mathrm{K}}$-point where a linear band structure can be observed. (c,d) The π-bands in the vicinity of the $\overline{\mathrm{K}}$-point for ideal (c) monolayer graphene (projected from panel (b)) and (d) bilayer graphene as calculated from a tight binding approach [22]. Whereas monolayer graphene shows a linear dispersion, bilayer graphene exhibits a parabolic spectrum. Both systems are a zero-gap semiconductor or a zero-overlap semimetal.

two-dimensional Brillouin zone of graphene in form of a hexagon and its high-symmetry points are sketched in panel (b) of the figure. The corners of this Brillouin zone are of particular importance for the physics of graphene. Due to the two graphene sublattices these corners of the Brillouin zone are the $\overline{\mathrm{K}}$- and $\overline{\mathrm{K}'}$-point, respectively and are often designated as different "valleys".

The remaining fourth electron in the p_z-orbital forms covalent π-bonds with the adjacent carbon atoms. In the extended graphene layer these bonds result in a half filled π-band system, which is responsible for the conductivity of graphene. The detailed π-band structure as calculated from tight-binding calculations [1, 16, 17] is displayed in figure 2 (a). As the figure shows, the lower valence (π-) and the upper conduction (π^*)-band meet each other at the $\overline{\mathrm{K}}$- and $\overline{\mathrm{K}'}$-points. This crossing point is called the Dirac point. Its energy position ($\mathrm{E_D}$, Dirac energy) is exactly at the Fermi level ($\mathrm{E_F}$). As the involved electrons belong to two different sublattices, an energy gap is not opened. Consequently, graphene can be seen as a zero-gap semiconductor or as a zero-overlap semimetal. As highlighted by the zoom in figure 2 (b), the π-bands display a linear dispersion around the Dirac point [1]. Thus, the electron transport is governed by Dirac's (relativistic) equation which leads to a number of unconventional effects such as new varieties of the quantum Hall effect, or relativistic quantum mechanical effects [2, 3, 4, 18, 19, 20, 21].

While a graphene monolayer displays a linear π-band dispersion with vanishing carrier density at the Dirac point as plotted in figure 2 (c), a bilayer system

exhibits a parabolic spectrum. Figure 2 (d) depicts the π-band system for an ideal bilayer as calculated from a symmetric tight-binding Hamiltonian following McCann and Fal'ko [22]. The π-band parabolas touch each other at the Dirac energy, so that this system is also a zero-overlap semimetal. We note, that an asymmetric electrostatic field perpendicular to the bilayer plane would open a band gap in its π-band system [22, 23, 24], which corresponds to the presence of an on-site Coulomb interaction in the theoretical description, as will be discussed in more detail in Section 3.3. The parametrization of the theoretical model will also be presented there.

The unconventional two-dimensional electron gas properties of graphene have been discovered primarily using flakes obtained from mechanical exfoliation from highly-oriented pyrolytic graphite [2, 3]. However, these flakes have to be searched for and manipulated individually which makes up-scaling towards wafer production cumbersome. Other methods of graphene production, e.g. by chemical derivation [10] have not provided high-quality single crystalline material, while the deposition by catalytic reaction or chemical vapor deposition on metal surfaces [9, 25, 26, 27] – unpractically – yield the graphene on a conducting substrate. On SiC, in contrast, growth of graphene can be achieved relatively simple by a thermal decomposition reaction and the layers are immediately provided on a large scale, semiconducting substrate, which is compatible to industrial wafer technology [28, 29, 30, 31, 32]. Different methods have been put forward for growth of epitaxial graphene on SiC. It is known for a long time that annealing of SiC basal plane substrates leads to a graphitization of the surface due to the enhanced sublimation of Si [33, 34]. This technique has ultimately been developed to prepare epitaxial graphene monolayers in ultra-high vacuum (UHV) on SiC(0001), the so-called Si-face of SiC, at typical temperatures in the 1200 °C regime [29, 30, 35]. We note, that in a similar UHV preparation, epitaxial graphene can also be obtained on SiC($000\bar{1}$), the so-called C-face [5, 28]. However, on the C-face it seems much more difficult to control the number of layers during growth. Unfortunately, the homogeneity of the graphene layers grown by the UHV method is somewhat limited – on both faces. On the C-face, de Heer and co-workers moved early to a furnace growth technique combined with an inert gas flow at higher temperatures which yielded graphene from monolayers to thick slabs [5]. In order to grow homogeneous mono- and few-layer graphene on SiC(0001), a suitable approach is to anneal the SiC samples at temperatures above 1600 °C in an Ar atmosphere in a quartz glass reactor [31, 36]. Furthermore, it has recently been demonstrated that it is also possible to grow graphene with an additional carbon supply similar to molecular beam epitaxy using relatively low temperatures of around 950 °C [37, 38] – this again on both SiC basal plane surfaces.

The present paper reviews recent work on the initial growth of graphene on SiC(0001) as well as tuning the electronic properties by surface functionalization: on SiC(0001), graphene growth is mediated by a covalently bound carbon interface layer, whose structural details will be discussed in detail. The strong interaction imposed by this interface ensures a very well ordered epitaxial relationship between the substrate and

graphene. On this surface also the growth of different numbers of graphene layers can be achieved and controlled precisely [29, 39, 40] as will be shown in addition. However, the interface, though responsible for the controlled epitaxy, represents a serious drawback for the use of epitaxial graphene on SiC(0001). The epitaxial graphene layers are intrinsically n-doped to a carrier concentration of approximately $n \approx 1 \times 10^{13}\mathrm{cm}^{-2}$ so that the Fermi level is shifted upwards, away from the Dirac point, or in other words the π-bands are shifted into the valance band regime [29, 40]. Thus, the ultimate goal for a wide-spread use of SiC based epitaxial graphene must be to reverse this Fermi level shift. Transfer doping by Sb or Bi deposition indeed reduces the n-doping to a certain extent, yet, not entirely [41]. Complete charge neutrality can be achieved by deposition of the strongly electronegative tetrafluoro-tetracyanoquinodimethane (F4-TCNQ) molecule [42]. In epitaxial bilayer graphene where the influence of the interface opens up a band gap, the Fermi level can be shifted into this band gap so that true semiconducting graphene develops. Even further, the size of the band gap is tuned by the electronic influence of the molecular layer. Details of this transfer doping process will also be shown.

Finally, we discuss how the influence of the interface bonding can be completely eliminated by hydrogen intercalation [13]. In this procedure, the dangling bonds of the SiC substrate are passivated with hydrogen so that the interfacial carbon layer is decoupled from the substrate. After the hydrogenation process linear π-bands appear even for this first carbon layer alone, that in its pristine state is electronically inactive. This so-called zerolayer is transformed into a quasi-free standing graphene monolayer. The intrinsically n-doped monolayer graphene transforms into a slightly p-doped bilayer graphene. No interfacial carbon bonds remain after hydrogen intercalation, in contrast to as-grown epitaxial graphene. The graphene decoupling is reversible by annealing to about 900 °C where the intercalated hydrogen atoms desorb.

2. Experiment

On-axis oriented 4H- and 6H-SiC(0001) samples doped with nitrogen (10^{17} to $10^{18}\,\mathrm{cm}^{-3}$ range) were initially prepared either by hydrogen etching [43, 44] in order to achieve a regular array of atomically flat terraces, or by a chemical-mechanical polishing (CMP) procedure. Growth of epitaxial graphene was carried out by a thermal decomposition reaction that initiates Si sublimation either by annealing in UHV [30] or under Ar atmosphere in an induction furnace [31]. Sample annealing in UHV was carried out by direct current or electron bombardment heating. The sample temperature was measured by an infrared pyrometer. For transfer doping, F4-TCNQ molecules (7,7,8,8-Tetracyano-2,3,5,6-tetrafluoroquinodimethane, Sigma Aldrich, 97% purity) were deposited on the graphene surfaces by thermal evaporation from a resistively-heated crucible in UHV. For hydrogen intercalation the samples were annealed at temperatures between 600 °C and 1000 °C in molecular hydrogen at atmospheric pressures. This process was carried out in a quartz-glass reactor in an atmosphere of palladium-purified ultra-pure molecular

hydrogen, similar to the technique used for hydrogen etching [43, 44] and hydrogen passivation [45, 46, 47] of SiC surfaces.

The graphene layer thickness and the shape and position of the π-bands were characterized using low energy electron diffraction (LEED) and angular resolved photoemission spectroscopy (ARPES). In house ARPES experiments were carried out at room temperature (RT) using monochromatic He II radiation ($h\nu = 40.8$ eV) from a UV discharge source with the dispersion measured by means of a display analyzer oriented for momentum scans perpendicular to the $\overline{\Gamma K}$-direction of the graphene Brillouin zone. For a precise determination of the carrier concentration the Fermi surfaces were measured via low temperature ARPES at the Surface and Interface Spectroscopy beamline (SIS) using synchrotron radiation from the Swiss Light Source (SLS) of the Paul Scherrer Institut (PSI) in Villigen, Switzerland [48]. By using a display analyzer and a liquid He cooled sample manipulator with three rotational degrees of freedom, the endstation allows for fast high-resolution, two-dimensional electronic dispersion measurements. X-ray photoelectron spectroscopy (XPS) measurements were performed using photons from a non-monochromatic Mg K_α source ($h\nu = 1253.6$ eV). High-resolution core level photoemission spectroscopy (CLPES) was carried out using synchrotron radiation at beamline I311 [49] of the MAX radiation laboratory in Lund, Sweden. Low energy electron microscopy (LEEM) and photoemission electron microscopy (PEEM) experiments were performed with the LEEM III instrument at this beamline.

3. Results

3.1. The ($6\sqrt{3}\times 6\sqrt{3}$)R30° phase as interface layer

A number of ordered phases are stable on the SiC(0001) surface, ranging from silicon rich to carbon rich surface composition [50]. For graphene preparation under UHV conditions, the optimum process [30, 35] starts with a hydrogen etched sample and the preparation of the Si rich (3×3) phase [51]. Subsequent annealing of this surface ($\approx$ 950 °C) leads to a ($\sqrt{3}\times\sqrt{3}$)R30° phase, which consists of a 1/3 monolayer of Si adatoms on top of the SiC substrate layers [52]. From further annealing to temperatures around 1100 - 1150 °C a well ordered ($6\sqrt{3}\times 6\sqrt{3}$)R30° phase develops [30, 35]. In this phase the SiC substrate is covered by an initial carbon layer [13, 53, 54]. A LEED pattern of this phase is displayed in figure 3 (a). The complex spot arrangement in this LEED pattern has triggered interpretation in various ways, such as resulting from a phase coexistence [55], a (6×6) nanomesh [56], or as a Moiré pattern of graphite and the SiC substrate both in (1×1) [28, 33] or ($\sqrt{3}\times\sqrt{3}$)R30° [57] periodicity. Indeed, most spot groups have an internal distance of 1/6 of the reciprocal unit vector of SiC. Depending on the preparation, even spots on a (5×5) grid appear [30]. Note,that in the LEED pattern of figure 3 (a) these (5×5) domains are practically absent. Some remaining domains of the ($\sqrt{3}\times\sqrt{3}$)R30° phase are present as indicated by the (1/3 1/3) spot. The sketch in figure 3 (b) highlights the different spot classes originating from the substrate, a

$(\sqrt{3}\times\sqrt{3})$R30°-, a (6×6)-, a (5×5) and the $(6\sqrt{3}\times6\sqrt{3})$R30°-grid [58], as discussed in detail in ref [30]. A close inspection reveals that the LEED pattern truly reflects a $(6\sqrt{3}\times6\sqrt{3})$R30° periodicity [30, 33, 35]. The large unit cell of the $(6\sqrt{3}\times6\sqrt{3})$R30° reconstruction evolves due to the different lattice parameters of graphene (2.46 Å) and the SiC substrate (3.08 Å). The reciprocal unit vectors of graphene and a SiC-bilayer are indicated in figure 3 (a) and (b) in red and green, respectively. Note, that the first order spot of graphene is only on the $(6\sqrt{3}\times6\sqrt{3})$R30°-grid, not on the (6×6)-grid. The combined layers form the coincidence superstructure of $(6\sqrt{3}\times6\sqrt{3})$R30° periodicity. This would be compatible with the interpretation as a Moiré pattern. However, the high LEED intensities found for the fractional order spots clearly indicate that the

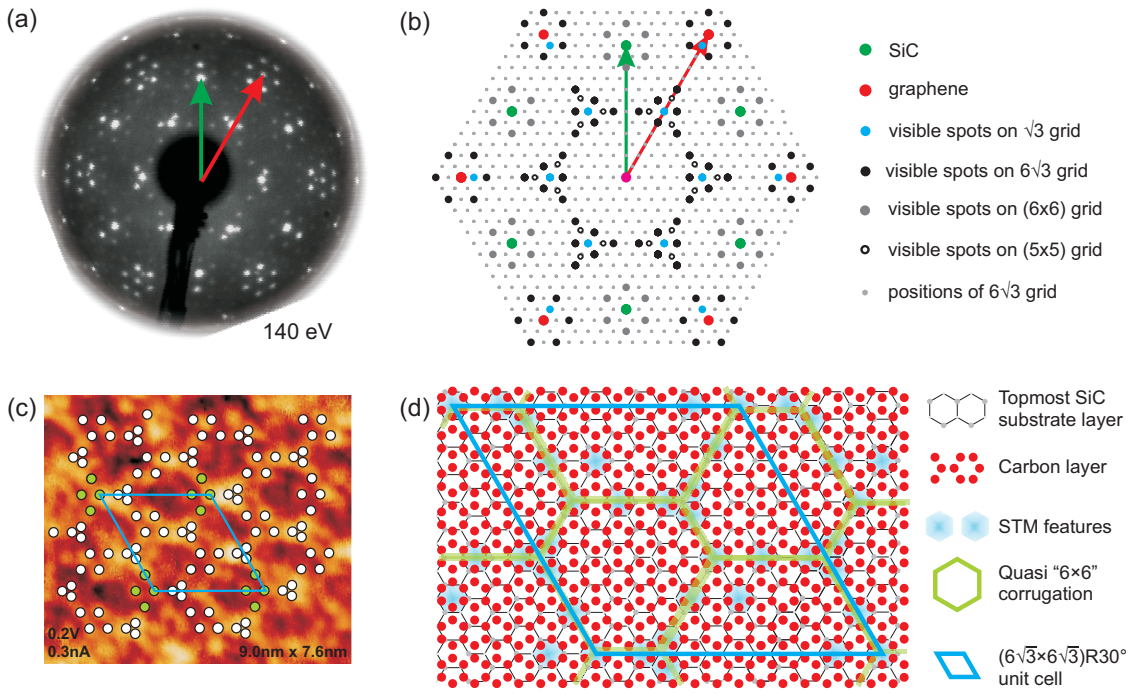

Figure 3. (a) LEED pattern of the $(6\sqrt{3}\times6\sqrt{3})$R30° reconstruction at 140 eV, with reciprocal unit vectors indicated, one each for SiC (green) and graphene (red). (b) Sketch of the different diffraction spots seen within the $(6\sqrt{3}\times6\sqrt{3})$R30° LEED pattern, originating from four different grids: the $(6\sqrt{3}\times6\sqrt{3})$R30° grid, the (6×6) grid, the $(\sqrt{3}\times\sqrt{3})$R30° grid and the (5×5) grid. Only the brightest spots of the LEED pattern in panel (a) are highlighted. (c) Atomically resolved STM image of the $(6\sqrt{3}\times6\sqrt{3})$R30° reconstruction of 4H-SiC(0001) (U_{tip} = 0.2 V), exhibiting rings of two different sizes within the $(6\sqrt{3}\times6\sqrt{3})$R30° unit cell. A sketch of the atom-like protrusions visible in STM and the $(6\sqrt{3}\times6\sqrt{3})$R30° unit cell are superimposed. (d) Structural model of the $(6\sqrt{3}\times6\sqrt{3})$R30° reconstruction in top view showing the Si-terminated (1×1)-SiC substrate and the graphene-like lattice of the initial carbon layer. The $(6\sqrt{3}\times6\sqrt{3})$R30° unit cell and the three hexagons in quasi-(6×6) periodicity are indicated. The blue shaded features along the walls of the quasi-(6×6) honeycomb depict the atom-like features observed in the STM image in panel (c).

$(6\sqrt{3}\times6\sqrt{3})$R30° surface is heavily reconstructed, e.g. by a significant buckling of the atoms in one or both layers.

STM images of the $(6\sqrt{3}\times6\sqrt{3})$R30° phase typically show a corrugation with an apparent (6×6) periodicity [30, 35, 55, 56, 59]. Low bias STM images often do not allow to identify a periodic arrangement of the surface atoms. However, under certain tip conditions, the true $(6\sqrt{3}\times6\sqrt{3})$R30° structure can indeed be resolved [30, 60]. An STM micrograph obtained with 200 mV tunneling bias [58] is shown in figure 3 (c). The STM image reveals rings in a distance corresponding to the quasi-(6×6) periodicity, as it is normally observed. However here, two types of rings with slightly different size are resolved. As indicated by the schematics superimposed to the STM image, three atom-like protrusions are only present in the larger rings (every third ring). Each protrusion is part of a diamond of four positions (marked in green in the figure), which – in the same orientation – is repeated only within the $(6\sqrt{3}\times6\sqrt{3})$R30° periodicity. Thus, one large and two smaller rings together form the true $(6\sqrt{3}\times6\sqrt{3})$R30° unit cell. Of course, the sketch drawn on top of the STM image resolves only a few atoms of the $(6\sqrt{3}\times6\sqrt{3})$R30° surface, its complete atomic structure is still unresolved. This fact, however, should not come as a surprise since the side length of one $(6\sqrt{3}\times6\sqrt{3})$R30° unit cell amounts to 32 Å. Consequently, the $(6\sqrt{3}\times6\sqrt{3})$R30° unit cell contains 108 Si and 108 C atoms per SiC bilayer and 338 atoms in a graphene layer. The $(6\sqrt{3}\times6\sqrt{3})$R30° unit cell on SiC is equivalent to a (13×13) graphene unit cell. This becomes more apparent in a top view sketch as shown in figure 3 (d). The schematic model gives more insight into the registry relation between the SiC substrate and the initial carbon layer. The quasi-(6×6) honeycomb hexagons with slightly varying size are highlighted in green, the true $(6\sqrt{3}\times6\sqrt{3})$R30° periodicity is indicated in blue. The light blue shaded areas mark the protrusions observed in the STM image of panel (c). They are distributed along the walls of the quasi-(6×6) honeycomb structure and are situated exactly on (1×1) SiC-substrate grid positions. The appearance of these protrusions reflects the strong reconstruction which was deduced from the LEED intensities.

As a result of this intense reconstruction the linear π-bands typical for graphene do not exist for this initial carbon layer [13, 53, 54]. Figure 4 (a) displays the band structure of the $(6\sqrt{3}\times6\sqrt{3})$R30° reconstruction around the $\overline{\mathrm{K}}$-point of the graphene Brillouin zone as measured by ARPES using He II excitation [13]. The measurements are taken perpendicular to the $\overline{\Gamma\mathrm{K}}$-direction. The sketch on the left defines the $\vec{k}_{\parallel}$-mapping direction. Indeed, no π-bands are visible. Instead, only two very faint delocalized and smeared out states at binding energies of around 0.1 eV to 0.5 eV and higher than 0.9 eV are visible that have been attributed to surface states of the $(6\sqrt{3}\times6\sqrt{3})$R30° reconstruction [53]. The suppression of graphene related properties in this layer is also confirmed from CLPES data measured at the MAX-Lab synchrotron [61]. Figure 4 (b) shows the C 1s core level signal with different components contributing to the spectra determined by a curve fitting procedure [58]. Besides the SiC bulk peak at 283.73 eV, two additional components called S1 at 284.99 eV and S2 at 285.60 eV can be identified. Neither component S1 nor component S2 is located at the position expected

for graphene, which would be at 284.7 eV. Consequently, the $(6\sqrt{3}\times6\sqrt{3})$R30° structure consists of two inequivalent non-graphene-like types of carbon atoms. Considering the $(6\sqrt{3}\times6\sqrt{3})$R30° structure as an initial carbon layer that is partially covalently bound to the substrate, they can be attributed to the following origin [53, 54]: S1 results from the carbon atoms in the $(6\sqrt{3}\times6\sqrt{3})$R30° structure bound to one Si atom of the SiC(0001) surface and to three C atoms in the sp^2-bonded layer, S2 is the component emitted from the remaining sp^2-bonded carbon atoms in the buffer layer. The two components have an area ratio S1:S2 of slightly below 1:2, i.e. almost 1/3 of the carbon atoms in the initial carbon layer are bound to the SiC substrate.

The experimental information from LEED, STM, ARPES, and CLPES allow to draw a structural model of the $(6\sqrt{3}\times6\sqrt{3})$R30° reconstruction, which is sketched in figure 4 (c). The interface layer represents an initial carbon layer in a graphene-like honeycomb arrangement and is partially covalently bound to the Si-terminated substrate. The bonds indicated in figure 4 (c) should be regarded as possible bond formations since not all Si atoms can form a bond to carbon atoms, due to the different lattice constants of SiC and graphene and due to the 30° rotation angle of the initial carbon layer with respect to the substrate. The covalent bonding breaks the hexagonal network of π-orbitals but preserves the σ-bonds [53, 62].

Recently, two DFT studies [62, 63] could shed further light onto the discrepancy between the (6×6) and $(6\sqrt{3}\times6\sqrt{3})$R30° periodicity of the interface layer. Topographic [62, 63] and charge density maps [62, 63] exactly exhibit the quasi-(6×6) periodicity with the two types of hexagonal rings observed in STM. In the calculations, the valleys of the quasi-(6×6) honeycomb are attributed to carbon atoms covalently

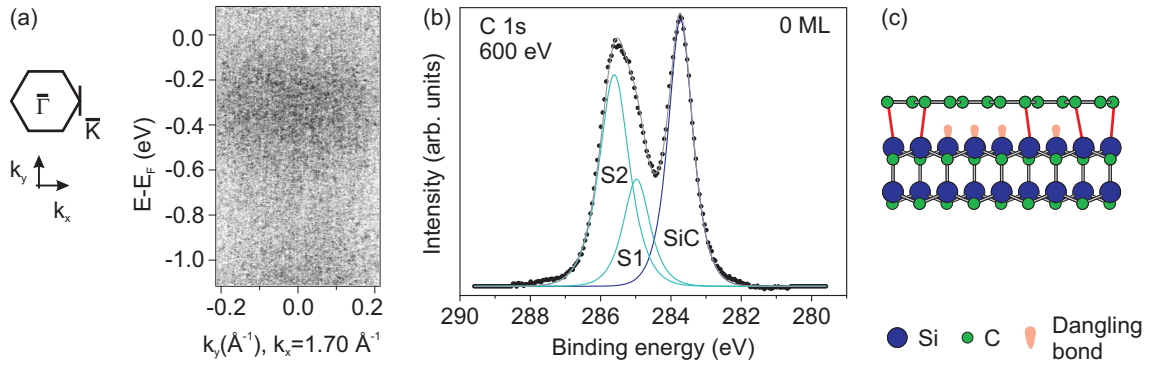

Figure 4. (a) Inverse grayscale plot of the band structure of the $(6\sqrt{3}\times6\sqrt{3})$R30° reconstruction near the $\overline{\text{K}}$-point obtained by ARPES using He II radiation. The measurement direction perpendicular to the $\overline{\Gamma\text{K}}$-line is indicated with the graphene Brillouin zone on the left. (b) C 1s spectrum of the $(6\sqrt{3}\times6\sqrt{3})$R30° reconstruction measured with an incident photon energy of 600 eV [61] and its deconvolution into different carbon components [58]. (c) Structural model of the $(6\sqrt{3}\times6\sqrt{3})$R30° phase in side view. It consists of a covalently bound initial carbon layer that does not yet exhibit the typical properties of graphene. Possible (unknown) atomic displacements due to the reconstruction are not shown.

bound to the SiC substrate, the walls of the quasi-(6×6) structure are claimed not to arise from Si dangling bonds but from carbon atoms that are not bonded to the SiC substrate and therefore pushed out of the plane.

3.2. Growth and layer counting

As we have shown above, the $(6\sqrt{3}\times6\sqrt{3})$R30° reconstruction represents a precursor stage of graphitization and is therefore often called "zerolayer graphene" [13, 64]. It serves as an interface or buffer layer for the epitaxial growth of true graphene layers. As mentioned in the introduction there are several different procedures available for the growth of epitaxial graphene on SiC(0001) [29, 30, 31, 37]. However, for all of these methods, the graphene growth is mediated by the $(6\sqrt{3}\times6\sqrt{3})$R30° reconstructed interface layer. Only the next carbon layer on top of this layer can be named monolayer graphene. During the graphene growth the $(6\sqrt{3}\times6\sqrt{3})$R30° structure is buried below the graphene layers. However, it is shown in this section that it still does have a significant electronic influence on the graphene. Concerning the graphene growth it should be considered that new graphene layers are formed due to the desorption of Si atoms. From a simple count of the carbon atoms, it is evident that three SiC bilayers are needed to form one graphene layer. As a new graphene layer has to be built from the bulk material, it has recently been assumed that the growth of an additional graphene layer implies the renewed formation of the $(6\sqrt{3}\times6\sqrt{3})$R30° reconstruction [54]. Simultaneously, the previous $(6\sqrt{3}\times6\sqrt{3})$R30° structure is released from its covalent bonding to the substrate and is transformed into a true graphene layer. In this way, all graphene layers are forced to have the same 30° rotation with respect to the substrate.

The fact that the $(6\sqrt{3}\times6\sqrt{3})$R30° reconstruction remains intact for a different number of graphene layers can clearly be demonstrated from CLPES data. Figure 5 shows the C 1s core level signal measured at 600 eV incident photon energy for epitaxial monolayer (a) and bilayer (b) graphene [65]. The data were acquired [61] and analyzed [66] in the same way as in figure 4 (b). In comparison to zerolayer graphene (figure 4 (b)) the C 1s peak for monolayer graphene in figure 5 (a) can only accurately be fitted after introducing a fourth component (G), which arises from the graphene overlayer. This component increases in intensity for higher graphene coverage as shown for bilayer graphene in figure 5 (b). The intensity ratio of the interface related components S1 and S2 to the SiC bulk component, however, hardly changes, which means that the $(6\sqrt{3}\times6\sqrt{3})$R30° structure is covered by the graphene layers but is otherwise not altered. Notably, the graphene peak shifts towards lower binding energy with increasing number of layers, in good correlation to the shift of the band structure due to the intrinsic n-doping of epitaxial graphene as shown below.

The Si 2p peak measured at 330 eV incident photon energy [61] is shown in figure 5 (c) for a graphene monolayer. Due to spin orbit splitting, the pure Si 2p peak already consists of two components, Si $2p_{1/2}$ and Si $2p_{3/2}$. Besides the SiC bulk peak, the line

shape analysis [66] reveals a component at the higher binding energy side attributed to the Si atoms of the substrate that bind to the carbon atoms of the $(6\sqrt{3}\times6\sqrt{3})$R30° reconstruction [67]. As they are still in sp^3-hybridization, only a small chemical shift with respect to the bulk peak, possibly due to strain, can be observed. A further peak at the lower binding energy side can be attributed to stem from surface defects [67]. While the data shown were measured from UHV prepared graphene layers, this peak is absent for samples, which are prepared by the furnace method under Ar atmosphere [31], and consequently have higher quality and a large-scale homogeneity. Figure 5 (d) displays

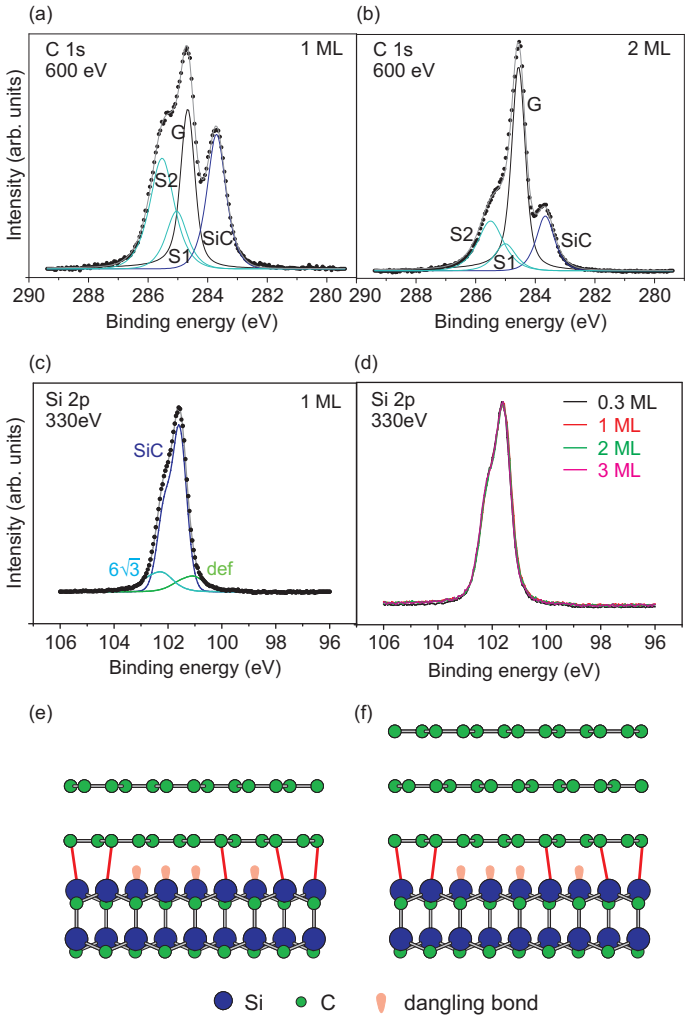

Figure 5. C 1s spectrum for (a) mono- and (b) bilayer epitaxial graphene together with their deconvolution into bulk (SiC), graphene (G) and $(6\sqrt{3}\times6\sqrt{3})$R30° reconstruction (S1 and S2) related components. The incident photon energy is 600 eV. (c) Si 2p spectra for monolayer epitaxial graphene together with the deconvolution into bulk (SiC), $(6\sqrt{3}\times6\sqrt{3})$R30° reconstruction $(6\sqrt{3})$ and defect (def) related components. The incident photon energy is 330 eV. (d) Si 2p spectra for different graphene coverages. Structural model of (e) monolayer and (f) bilayer epitaxial graphene on SiC(0001) in side view. The graphene is growing on top of the $(6\sqrt{3}\times6\sqrt{3})$R30° reconstructed interface layer.

the Si 2p spectrum for varying graphene coverage with normalized intensities. The spectral shape is practically identical for all coverages, which corroborates that the bonding configuration at the interface is independent from the number of graphene layers grown. Accordingly, the structural model for the interface layer as drawn in the previous section, cf. figure 4 (c) can be extended to the mono- and bilayer situation as displayed in figure 5 (e,f) with the graphene layers arranged on top of the further buried, but identical interface.

An important aspect of the growth of epitaxial graphene on SiC(0001) is the precise control and counting of the number of graphene layers obtained. Using CLPES data such as the ones shown in figure 5 this can be achieved only with limited accuracy. For a precise control of the growth results, photoemission spectroscopy of the π-bands is the most direct method available, since for a different number of graphene layers a different number of π-band branches evolves as seen in the introduction. We note, that on SiC(0001) the number of graphene layers developing is dependent on the annealing temperature. Figure 6 (a and b) shows in house ARPES measurements (He II radiation) for annealing temperatures of 1200 °C and 1350 °C. As for the band structure shown in figure 4 (a) (after annealing at $\approx$ 1150 °C), the measurements are taken at the $\overline{\mathrm{K}}$ point perpendicular to the $\overline{\Gamma\mathrm{K}}$-direction, cf. sketch in figure 4 (a). As we have seen, for 1150 °C annealing temperature the $(6\sqrt{3}\times6\sqrt{3})$R30° reconstructed interface layer develops, and accordingly no bands are visible, cf. figure 4 (a). For higher annealing

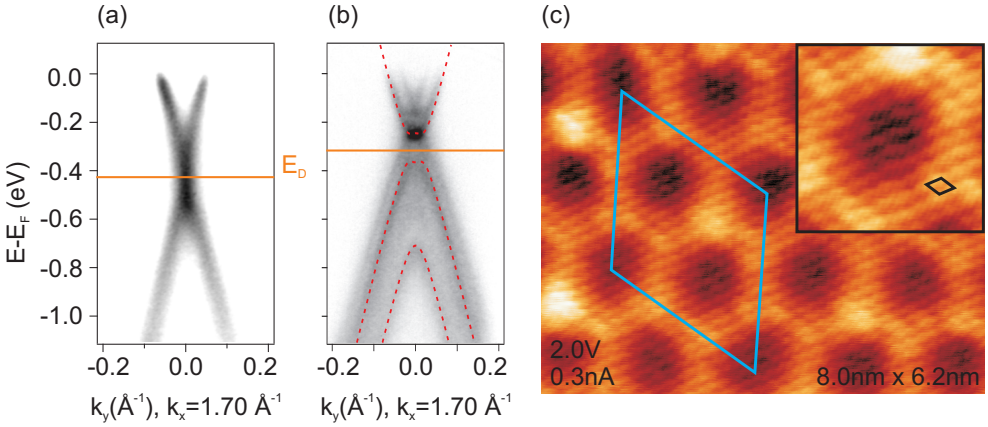

Figure 6. (a, b) Layer counting of epitaxial graphene on SiC(0001) by π-band analysis from photoemission (ARPES) images of the valence band structure measured at the $\overline{\mathrm{K}}$ point of the graphene Brillouin zone obtained using He II radiation (measurement direction perpendicular to the $\overline{\Gamma\mathrm{K}}$-line as indicated in Figure 4). (a) One π-band branch indicative for monolayer graphene with the position of the Dirac energy at -420 meV indicated. (b) Bilayer graphene with two π-band branches together with fitted spectral functions from tight-binding calculations. The Dirac energy is located at -300 meV. (c) High resolution STM micrograph of epitaxial graphene on 4H-SiC(0001) (U_{tip} = 2.0 V). The graphene latticed is imaged with atomic resolution (see inset and black unit cell). Overlayed to the graphene lattice is the quasi (6×6) ring structure imposed from the interface corrugation. The $(6\sqrt{3}\times6\sqrt{3})$R30° unit cell is indicated in blue.

temperatures graphene layers are obtained, that can be characterized by the number of π-band branches in the dispersion plot. As shown in figure 6 (a) the monolayer shows the typical crossing of linear bands. Notably, the energy level of this crossing, i.e. the Dirac point is located at -420 meV, which corresponds to the noted strong n-doping of $n \approx 1 \times 10^{13}\,cm^{-2}$. This doping effect is independent of the preparation procedure, as well as of polytype and doping level of the substrate. As shown in panel (b) for a bilayer two parabolic band branches are observed. Here, the band shift caused by the n-doping is slightly lower than for epitaxial monolayers, namely about -300 meV. Theoretical bands from tight-binding calculations fitted to the data show that in addition a band gap of roughly 100 meV is opened which corroborates that the electric dipole present at the graphene/SiC interface imposes an electrostatic asymmetry between the layers [29, 39, 40, 68]. ARPES can be thus used to control that a defined number of layers is obtained, since an inhomogeneous layer distribution is reflected in a superposition of the different band structures. Note, that the bilayer sample indeed contains residual amounts of trilayer graphene.

The intrinsic doping even for more than one graphene layer is caused by the persistent influence of the interface. This influence can also be demonstrated from STM measurements. For certain tip conditions the graphene layer can be imaged with atomic resolution in room temperature STM experiments as shown in figure 6 (c). The graphene layer was prepared by annealing around 1300 °C. The inset in the figure shows the atomically resolved graphene lattice in detail. The unit-cell of about 2.5 Å is indicated. Since we observe only one of the two carbon atoms within the graphene unit cell, we identify this surface region as bilayer graphene [30], which corresponds also well to the preparation temperature. The Bernal stacking of two graphene sheets leads to the observation of such a diamond-shaped lattice [69]. However and more important, also clearly visible is a variation of the tip height for constant tunneling current with the quasi-(6×6) corrugation of the interface layer. In the larger scale (full image) the $(6\sqrt{3}\times6\sqrt{3})$R30° unit cell is indicated containing the different rings that apparently influence the density of states in the graphene layer.

While ARPES facilitates an accurate method to count the graphene layers on top of SiC(0001), it is a complicated experiment, that is not always available. Preferable would be an accurate and at the same time easy and practical determination of the number of graphene layers. Indeed, by calibrating them to the ARPES data, LEED measurements can be used as a fast, *in-situ* growth control technique as previously shown [40]. We should note, that the calibration of the number of graphene layers from ARPES has been revised using more accurate measurements in the meantime [58] and is slightly different from the earlier publication [40]. During graphitization at increasing temperatures, the LEED pattern continuously undergoes variations visible by eye, in particular the spot intensity of the first diffraction order of graphene varies. In the LEED pattern displayed in figure 7 the (10) spot of the SiC substrate is indicated. The zoomed sketch to the right marks the (10) spot of the graphene lattice together with six surrounding diffraction spots of the $(6\sqrt{3}\times6\sqrt{3})$R30° reconstruction. As shown below

in the figure, the intensity spectrum of this graphene spot can be used as a fingerprint that allows for an exact thickness determination for at least zerolayer, monolayer, and bilayer graphene, so that the number of layers can be continuously monitored during the preparation process with high accuracy. The annealing temperature for the sample was identical to the ARPES measurements discussed above, i.e. 1150 °C, 1200 °C and 1350 °C. The features changing significantly in the spectra are emphasized by the yellow balloons. It may be argued, that not every LEED setup permits to record spot intensity spectra, but already a LEED pattern at 126 eV, taken at normal incidence, allows for an approximate determination of the number of layers by comparing the relative intensity of the graphene (10) spot to that of the surrounding spots in the $(6\sqrt{3}\times6\sqrt{3})$R30° pattern as also shown on the right side of figure 7. For the pure interface layer the graphene (10) spot is weaker than its surrounding spots, for monolayer graphene they approximately display the same intensity, and for bilayer graphene, the graphene spot is brighter than its surrounding spots. We note that epitaxial graphene on 4H-SiC(0001)

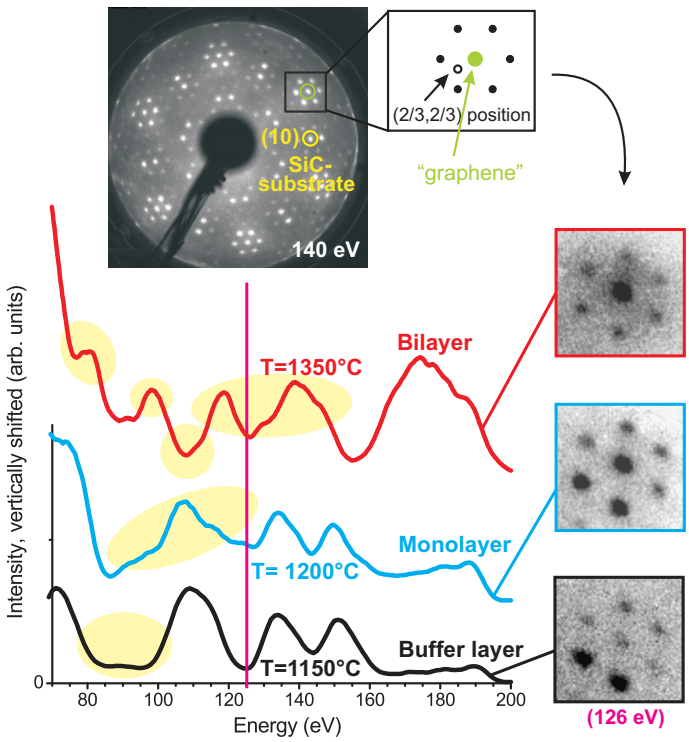

Figure 7. LEED spot intensity spectra for different numbers of epitaxial graphene layers grown (at the indicated temperatures) on 4H-SiC(0001). As indicated in the inset, the spectra were obtained for the green marked spot of the $(6\sqrt{3}\times6\sqrt{3})$R30° reconstruction, which is the graphene (10) spot. The first order diffraction spot for the SiC substrate is indicated in the LEED pattern in yellow, the position of the (2/3,2/3) spot of the $(6\sqrt{3}\times6\sqrt{3})$R30° reconstruction in the inset. Yellow patches indicate fingerprint like features in the spectra that allow the unambiguous determination of the number of graphene layers. LEED patterns at 126 eV are shown on the right, also allowing for a discrimination.

and 6H-SiC(0001) results in the same LEED spectra [70], a finding that corroborates that - at least with the same preparation procedure - the polytype has no influence on the structural and electronic properties of epitaxial graphene on SiC.

The number of layers can be analyzed accurately with high spatial resolution using LEEM, which can be used to identify the number of graphene layers on SiC by the number of dips in the electron reflectivity spectra between 0 and 8 eV [40, 71]. Also Raman spectroscopy allows the characterization of the graphene layer thickness [72]. It can also be used to analyze influences of strain, the carrier concentration and to detect defects in the graphene layers [42, 72, 73, 74, 75].

3.3. Transfer doping

In order to exploit many of the unique properties of graphene as semimetal also in SiC based epitaxial graphene, the intrinsic doping has to be reversed. This means that the electrons have to be extracted out of the graphene layer. A schematic sketch visualizes the band structure of monolayer epitaxial graphene on SiC(0001) for different doping levels in figure 8. Directly after growth, the graphene is intrinsically n-doped due to charge transfer from the substrate, as indicated in panel (b) of the figure. Extensive n-type doping can be induced very effectively by alkali atoms that easily release their valence electron [29, 76]. The Dirac point is shifted further into the occupied states away from the Fermi level as illustrated in figure 8 (a). Similarly, NH_3 has been used for enhanced n-doping [77]. In order to reach charge neutrality ($E_D \approx E_F$) for epitaxial graphene, p-doping must compensate the intrinsic n-doping. This situation is sketched in figure 8 (c), whereas panel (d) exemplifies the true p-type regime in order to round up the picture. A successful implementation of p-type doping is difficult. Nevertheless, as known from transport experiments on graphene flakes the carrier concentration changes already due to environmental influences. For a monolayer graphene sample that was exposed to air by taking it out of the UHV chamber, ARPES measurements show a Dirac energy of 260 meV below the Fermi level, cf. figure 9, instead of 420 meV as in a pristine epitaxial monolayer. Using this value, we obtain an electron concentration of

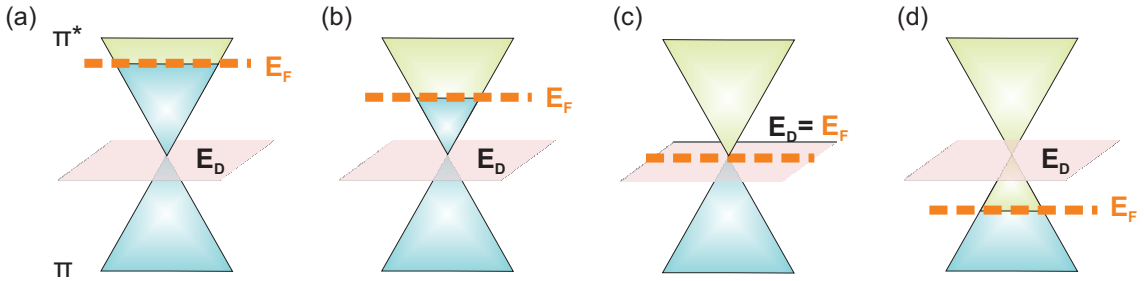

Figure 8. Position of the Dirac point and Fermi level of monolayer epitaxial graphene on SiC(0001) as a function of doping. Panel (a) stands for an n-doped monolayer, panel (b) for an as grown monolayer, panel (c) for a charge neutral monolayer, and panel (d) visualizes truly p-doped monolayer graphene.

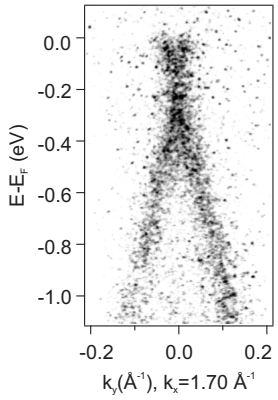

Figure 9. Band structure of epitaxial monolayer graphene after exposure to air as measured with ARPES (He II excitation). Due to p-type dopants the Dirac energy is shifted below the Fermi level only by 260 meV and not by 420 meV as for clean epitaxial monolayer graphene. The low quality of the image has to be attributed to contaminations from air.

$n \approx 4.2 \cdot 10^{12}$ cm^{-2}. The reduced electron concentration may be due to compensation by p-type dopants such as adsorbed oxygen, hydrocarbons or water molecules from the ambient environment (Note that the previously cooled sample had not been completely warmed up when the venting process was started.). The ARPES data shown here serve as a first proof of principle of the feasibility of p-type doping of epitaxial graphene. Indeed, injection of holes into graphene has been achieved via surface adsorption of NO_2 [77, 78, 79]. However, the high reactivity of NO_2, as well es of the above mentioned NH_3 and of alkali atoms makes those materials ill-suited as practical dopants. This is illustrated by the need of cryogenic temperatures and ultra high vacuum conditions to stably adsorb NO_2 or potassium on graphene surfaces [29, 79]. Heavier elements like Sb or Bi can be used for p-type transfer doping by deposition from a metal evaporator onto the epitaxial graphene surfaces. However, the effect is not sufficient to achieve charge neutrality [41].

A more promising approach is given by organic molecules [80, 81, 82]. Many of these molecules possess good thermal stability, have limited volatility after adsorption, and can be easily applied via wet chemistry. An effective p-type dopant is the strong electron acceptor F4-TCNQ. It is of great technological relevance as it plays an important role in optimizing the performance in organic light emitting diodes [83]. It only would be incompatible with high temperature processes. As noted, the doping level of the graphene layers can be precisely monitored with ARPES measurements of the π-band dispersion around the $\overline{\mathrm{K}}$ point of the graphene Brillouin zone as previously established [29, 39, 40, 68]. This is once more shown for an as-grown monolayer of graphene on SiC(0001) in figure 10 (a) where the Fermi level E_F is located about 420 meV above the Dirac point E_D (charge carrier concentration value of $n \approx 1 \times 10^{13}$ cm^{-2}). For increasing amounts of deposited F4-TCNQ, E_F moves back towards E_D as shown in panel (b) until charge neutrality is achieved for a nominal film thickness of 0.8 nm, cf. panel

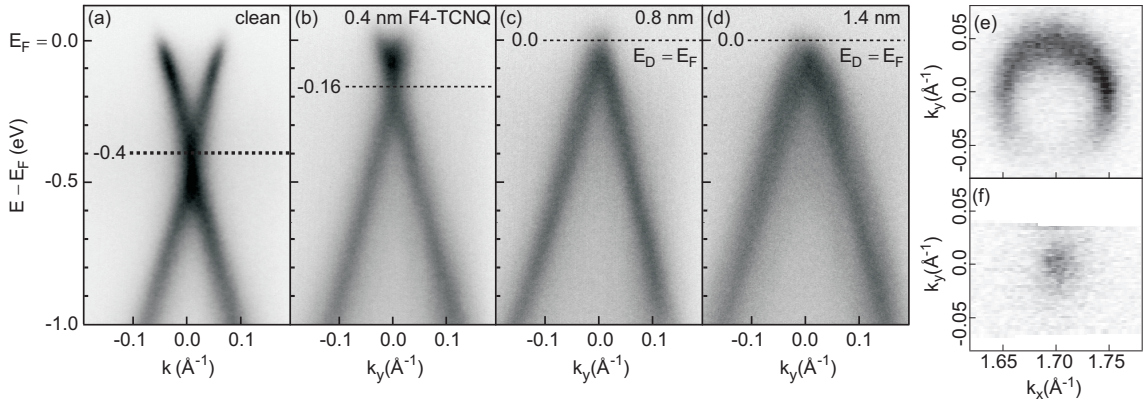

Figure 10. Dispersion of the π-bands at the $\overline{\mathrm{K}}$ point of the graphene Brillouin zone for (a) an as-grown graphene monolayer on SiC(0001), (b) after deposition of a partial F4-TCNQ film, (c) after saturation with F4-TCNQ molecules. The Fermi level $\mathrm{E_F}$ shifts back towards the Dirac point ($\mathrm{E_D}$, dotted black line) and charge neutrality ($\mathrm{E_F} = \mathrm{E_D}$) is reached. (d) π-band-dispersion after further growth of a second layer of F4-TCNQ with no further band shift observed. Fermi surface maps for (e) a pristine epitaxial graphene monolayer and (f) a F4-TCNQ covered charge neutral sample. The dispersion plots were measured using He II radiation (perpendicular to the $\overline{\Gamma\mathrm{K}}$-direction), the Fermi surfaces with 30 eV circular polarized synchrotron light (after [42]).

(c) [42]. The integrity of the graphene layer is preserved as indicated by the persistent sharpness of the bands. Evidently, deposition of F4-TCNQ activates electron transfer from graphene towards the molecule and compensates the intrinsic n-doping induced by the interface. At molecule coverages higher then 0.8 nm no further π-band shift is observed as shown in panel (d). Apparently, the charge transfer saturates. Figure 10 displays also constant energy maps at $\mathrm{E_F}$ as obtained from high-resolution ARPES data using synchrotron radiation for a clean graphene monolayer (e) and charge transfer saturation at full coverage (f). The charge carrier concentration can be derived precisely from the size of the Fermi surface pockets as $n = (k_\mathrm{F} - k_{\bar{\mathrm{K}}})^2/\pi$, where $k_{\bar{\mathrm{K}}}$ denotes the wave vector at the corner of the graphene Brillouin zone. The corresponding carrier concentrations as obtained from the synchrotron data are $7.3{\times}10^{12}$ cm^{-2} and $1.5{\times}10^{11}$ cm^{-2}, for the clean and the F4-TCNQ covered graphene monolayer, respectively. The error was estimated to about $\pm\ 2{\cdot}10^{11}$ cm^{-2} from the variance of Lorentzian fits through the corresponding dispersion plots [42].

How the charge transfer proceeds can be monitored by XPS measurements of the N 1s and F 1s core levels. A line shape analysis of the N 1s spectra for different amounts of deposited F4-TCNQ as plotted in figure 11 (a) reveals two main components at different binding energies, namely an anionic $\mathrm{N^{-1}}$ species (398.3 eV) and a neutral $\mathrm{N^0}$ species (399.6 eV) [84, 85]. An additional broad component observed at 401.7 eV can be assigned to shake-up processes [86]. In contrast to nitrogen, the F 1s spectra are dominated by a single component as shown in figure 11 (b). Only at low coverages a slight asymmetry develops. The appearance of the $\mathrm{N^{-1}}$ species indicates that the electron transfer takes

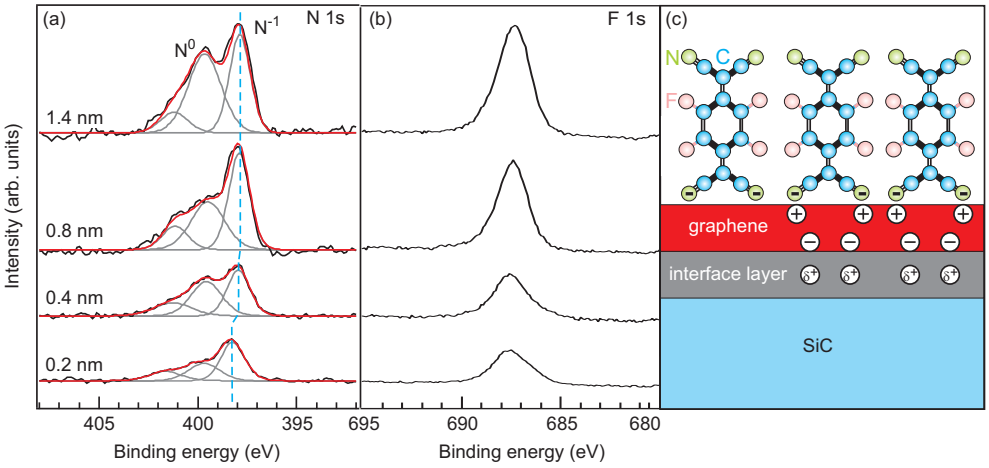

Figure 11. XPS spectra of the N 1s (a) and F 1s (b) core level emission regions from submonolayer (bottom spectrum) to multilayer (top spectrum) amounts of F4-TCNQ deposited on a monolayer of epitaxial graphene on SiC(0001). Three different components are fitted into the N 1s region and are assigned to N^{-1} and N^0 species and to a shake-up process. The blue dashed line indicates the exact energy position of the N^{-1} component as it shifts with molecular layer thickness. (c) Schematic structure of a F4-TCNQ layer deposited on top of a graphene layer grown on SiC. The charges induced in the graphene layer due to the interface dipole and the molecular charge transfer are indicated (after [42]).

place through the C≡N groups of the molecules while the fluorine atoms are largely inactive. Yet, not all C≡N groups are involved in the charge transfer process. While for low molecular coverages the charged species dominate (71%), for coverages from 0.4 nm to 0.8 nm about 45% of the cyano groups are uncharged as determined from the fitted peak areas. This indicates that at least when the films are densely packed, most of the molecules are standing upright or are upwards-tilted, as sketched in Fig. 11 (c). This is in difference to charge transfer complexes of F4-TCNQ on metal surfaces where all cyano groups are involved and the molecules lie flat [86, 87, 88]. The XPS peak positions also corroborate the close electronic coupling between the F4-TCNQ molecules and the graphene layer since for 0.8 nm film thickness their energy position shifts by exactly the same 0.4 eV as the π-bands. For higher film thicknesses a charge neutral second layer of molecules forms as indicated by the now dominant N^0 species in the N 1s spectra. The saturation effect at 0.8 nm thickness also supports the model of upright standing molecules since the size of an F4-TCNQ molecule along its axis is indeed about 0.8 nm.

Similar to the monolayer case, F4-TCNQ deposition onto a bilayer sample causes a progressive shift of the π-bands, i.e. a reduction of the intrinsic n-type doping. This is illustrated by the plots of experimental dispersion curves in figure 12 (a)-(d). In the figure, theoretical bands calculated from a tight-binding Hamiltonian [22] are superimposed to the dispersion plots. This facilitates an analytical evaluation of the Dirac energy position and the size of the band gap. Concurrent with the band structure shift, the size of the band gap increases. The band fitting retrieves the energy of the

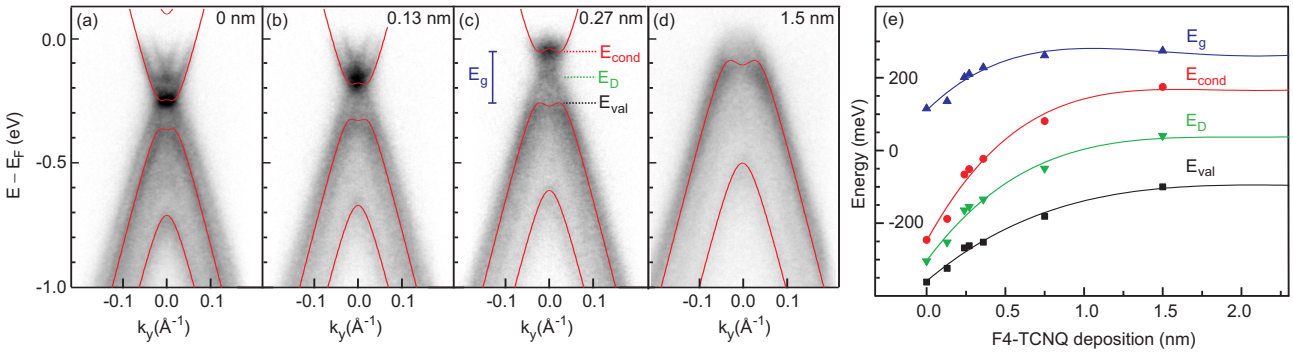

Figure 12. ARPES band structure plots measured perpendicular to the $\overline{\Gamma K}$-direction for an epitaxially grown graphene bilayer on SiC(0001) (a) without F4-TCNQ coverage and (b-d) with increasing amounts of F4-TCNQ. Bands calculated within a tight binding model are superimposed to the experimental data. (e) Evolution of the energy gap E_g, the gap midpoint or Dirac point E_D, the minimum of the lowest conduction band E_{cond} and the maximum of the uppermost valence band E_{val} as a function of molecular coverage. The evolution of the energies for higher molecular coverages (up to 5 nm, not shown) confirms the charge transfer saturation. The definition of the energies is included in panel (c). (after [42]).

bottom of the lowest conduction band E_{cond} and of the top of the uppermost valence band E_{val}. From these values the energy gap E_g and the mid gap energy or E_D can be derived. The corresponding energies are marked in panel (c). As displayed in panel (e), the band gap E_g increases from 116 meV for a clean as-grown bilayer to 275 meV when a 1.5 nm thick layer of F4-TCNQ molecules has been deposited. No further charge transfer is observed in the band structure measurements for higher amounts of deposited molecules (not shown). The conduction band maximum crosses the Fermi level for a molecular layer thickness of 0.4 nm. Hence the bilayer is turned from a metallic system into a truly semiconducting layer. The increase of the band gap indicates that the molecular deposition increases the on-site Coulomb potential difference between both layers. From the tight binding calculations we get an increase in the on-site Coulomb interaction from 120 meV for a clean bilayer to 290 meV for a bilayer with a molecular coverage of 1.5 nm. This increase can be attributed to an increased electrostatic field due to the additional dipole developing at the graphene/F4-TCNQ interface. For optimum reproduction of the experimental data the band velocity v_B equals 1.07×10^6 m/s. The dimer coupling γ varies from 400 meV for the clean bilayer to 520 meV for a bilayer with a molecular film coverage of 1.5 nm. The next-nearest neighbor coupling γ_3 remains fixed at 120 meV.

3.4. Hydrogen intercalation

While the transfer doping scheme reverses the intrinsic doping level of the epitaxial layers, the actual nature of the substrate/graphene interface is not changed. The interface layer is already constituted of carbon atoms arranged in a graphene-like

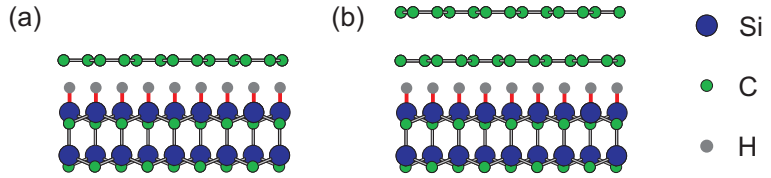

Figure 13. Side view models for quasi-free standing graphene after hydrogen intercalation under (a) the $(6\sqrt{3}\times6\sqrt{3})$R30° reconstruction of SiC(0001) ("zerolayer") and (b) an epitaxial monolayer graphene.

honeycomb structure. However as noted above, about 30% of these carbon atoms are bound to the substrate, which prevents linear π-bands as characteristic for graphene to develop in this layer, cf. figure 4. Thus, the interface layer is electronically inactive in terms of the typical graphene properties so that it is often called zerolayer graphene. Only the second carbon layer grown on top of the interface acts like monolayer graphene. In addition to inducing the intrinsic n-doping the covalent bonding in the interface is one of the primary suspects for the strongly reduced mobility in epitaxial graphene on SiC(0001) in comparison to exfoliated graphene flakes. So, for a practical application of epitaxial graphene on SiC(0001) instead of only counteracting the intrinsic doping it would be even better to eliminate the interface bonding completely by a saturation of the Si atoms in the uppermost SiC bilayer and thus to create quasi-free standing layers. This can be achieved by intercalation of hydrogen which breaks and saturates the respective bonds and thus structurally and electronically decouples the graphene layers from the substrate [13] as sketched for zero- and monolayer graphene in figure 13 (a) and (b). For this purpose the samples were exposed to molecular hydrogen ($\approx$ 950 mbar) at temperatures between 600 °C and 1000 °C typically for 10 min. [89]

LEED images provide a first estimate of the structural coupling between the epitaxial carbon layers and the substrate. Figure 14 displays LEED patterns at 126 eV for the $(6\sqrt{3}\times6\sqrt{3})$R30° reconstructed interface layer before and after hydrogen treatment, respectively. For this pristine zerolayer graphene sample (panel a) the

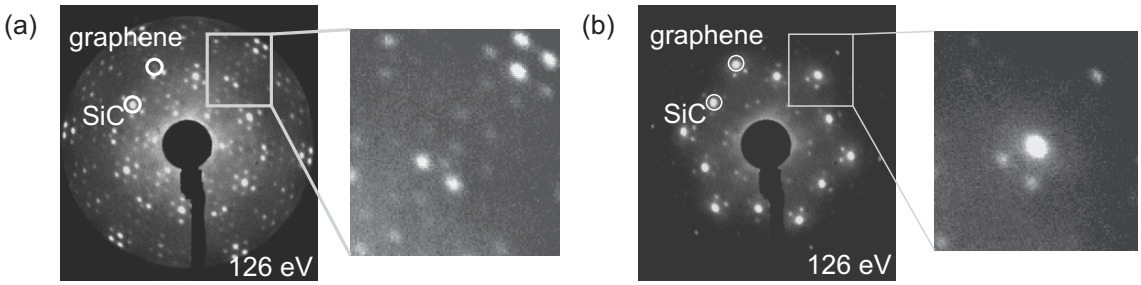

Figure 14. LEED patterns at 126 eV for (a) the $(6\sqrt{3}\times6\sqrt{3})$R30° reconstruction (so-called zerolayer graphene) of SiC(0001) and (b) the $(6\sqrt{3}\times6\sqrt{3})$R30° reconstruction after hydrogen intercalation. The first order diffraction spots are indicated for SiC and graphene. The intensity of the superstructure spots are displayed in the zoomed areas.

LEED pattern shows very intense $(6\sqrt{3}\times6\sqrt{3})$R30° superstructure spots, whereas, after hydrogen treatment (panel b), the superstructure spots are strongly suppressed and the first order diffraction spot of graphene becomes very bright. This indicates the transformation of a strongly reconstructed interface layer to a decoupled graphene-like flat layer induced by the elimination or weakening of the interlayer bonding. Similar to the case of a zerolayer, the spots of the $(6\sqrt{3}\times6\sqrt{3})$R30° superstructure vanish upon hydrogen treatment of an epitaxial graphene monolayer (not shown), again a clear indication of a structural decoupling of the interface layer from the substrate.

To demonstrate the electronic effect of the hydrogen treatment process, figure 15 shows ARPES measurements around the $\overline{\mathrm{K}}$ point of the graphene Brillouin zone [13]. As shown before for zerolayer graphene, i.e. the pristine $(6\sqrt{3}\times6\sqrt{3})$R30° reconstruction, no bands are observed (panel a). After hydrogen treatment the decoupling is clearly evident since the linear dispersing π-bands of monolayer graphene appear (panel b). This corroborates that the hydrogen atoms migrate under the covalently bound initial carbon layer, break the bonds between C and Si and bind to the Si atoms as sketched in figure 13 (a). Consequently, the zerolayer now displays the electronic properties of a quasi-free standing graphene monolayer. The graphene is slightly p-doped so that the Fermi level E_F is shifted below the Dirac point E_D by ≈ 100 meV in contrast to conventional epitaxial monolayer graphene which is n-doped. After heating the sample up to 700 °C the slight p-doping vanishes, presumably due to desorption of residual chemisorbed species from the graphene surface, and charge neutrality is retrieved as shown in figure

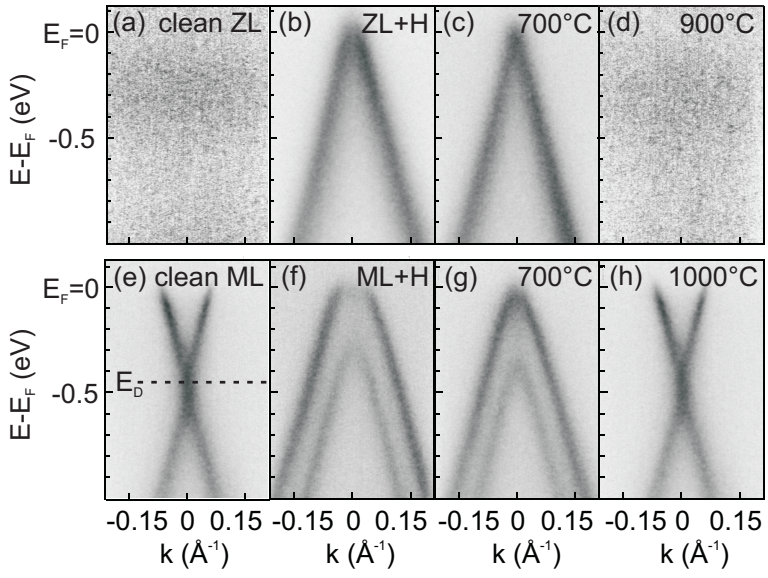

Figure 15. Dispersion of the π-bands measured with ARPES perpendicular to the $\overline{\Gamma\mathrm{K}}$-direction of the graphene Brillouin zone for (a) an as-grown graphene zerolayer (ZL) on SiC(0001), (b) after hydrogen treatment and subsequent annealing to (c) 700 °C and (d) 900 °C. π-band dispersion for (e) an as-grown monolayer (ML), (f) after hydrogen treatment and annealing to (g) 700 °C and (h) 1000 °C (after [13]).

15 (c). In Fermi surface measurements using high resolution, synchrotron based ARPES the charge carrier concentration could be evaluated to $n \approx 2 \times 10^{11}$ cm^{-2} [90]. At higher temperatures, the Si-H bonds start to break, and the hydrogen progressively desorbs. At around 900 °C the zerolayer structure is completely re-established as confirmed by ARPES, cf. figure 15 (d), which demonstrates that the hydrogen intercalation process is fully reversible. For pristine monolayer graphene, hydrogen treatment leads to the transformation into bilayer graphene as demonstrated by the change of the band structure displayed in figure 15 (e) and (f). It shows that the hydrogen intercalation process makes the interface layer and the first graphene layer on top combine to a bilayer slab in perfect AB stacking. Again, the sample shows p-doping which is reduced after annealing to 700 °C, cf. panel (g). From the fit of recent synchrotron data to tight binding calculations, we determined a hole carrier concentration in the range of $8 \cdot 10^{11}$ cm^{-2} to $1.8 \cdot 10^{12}$ cm^{-2}, corresponding to $E_F - E_D \approx 25$ - 35 meV [90]. According to the band fit, the band gap is practically closed ($\approx$ 30 meV in size). This means, that the electrostatic potential difference between the lower and upper layer which causes the gap in as-grown bilayers on SiC(0001) has vanished, which corroborates that the influence of the interface is largely absent in quasi-free standing epitaxial bilayer graphene. Again, for higher temperatures the intensity of the bilayer π-bands decreases while the monolayer bands reappear [13]. The hydrogen progressively desorbs until at 1000 °C the original monolayer band structure is completely recovered (panel h).

LEEM was employed to analyze the effect of hydrogen intercalation below epitaxial graphene with spatial resolution using the dip structure in the electron reflectivity spectra as measure for the number of graphene layers [71]. Figure 16 shows LEEM micrographs obtained on a sample with an intentionally inhomogeneous graphene coverage. The data were measured with an electron energy of 5.1 eV in the same area of the sample with (panel (a)) and without (panel (b)) intercalated hydrogen. At this energy, regions of different graphene thickness can be distinguished by the reflected intensity. The electron reflectivity spectra for the different surface domains A, B and C as labeled in panel (a) are plotted in panel (c). The number of dips in the spectra identifies region A, B and C as bi-, tri-, and four layer graphene. After desorbing the hydrogen through an annealing step at 900 °C, the spatial distribution of these domains does not change as shown in panel (b). However, their LEEM intensity changes and the reflectivity spectra as plotted in panel (d) identify a complete transformation of (n+1)-layer thick areas into (n)-layer thick areas (n=1,2,3). We note a small region in figure 16 that is labeled D. It displays the same intensity before and after desorption of the hydrogen (and a flat reflectivity spectrum) which we attributed to surface defects, e.g. from residual polishing damage [13]. Recent LEEM measurements after hydrogen intercalation of a furnace-grown zerolayer sample demonstrate that the combination of these two techniques allows to prepare continuous, homogeneous quasi-free standing monolayer graphene on a 10 μm scale [90]. High resolution CLPES experiments with synchrotron radiation and spatially resolved μ-XPS using the PEEM instrument give further evidence for the structural models given in figure 13. In the C 1s core level

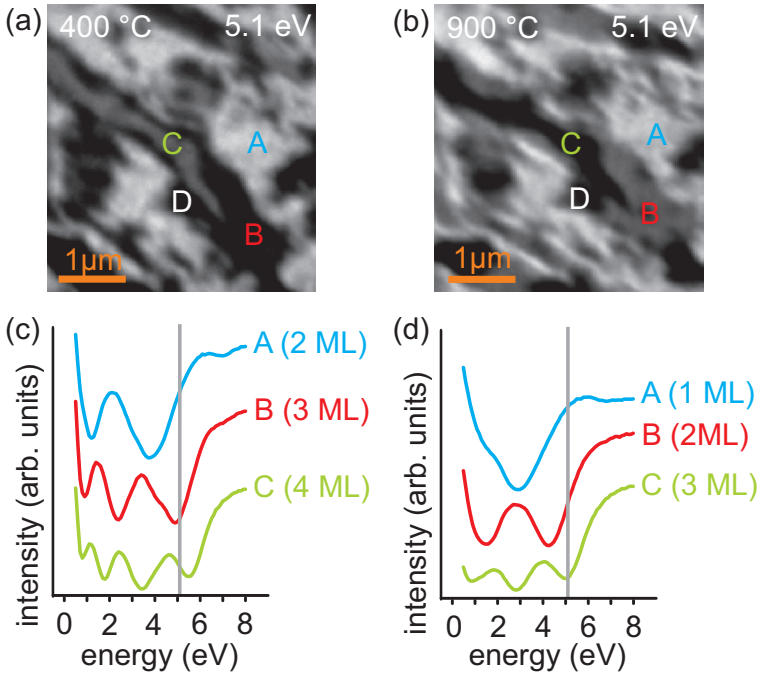

Figure 16. $4\times4\ \mu m^2$ LEEM micrographs recorded with an electron energy of 5.1 eV for the same area of (a) a hydrogen-treated graphene sample after outgassing at 400 °C and (b) annealed at 900 °C. Representative regions are labeled A, B, C, D. The electron reflectivity spectra obtained for the regions A, B, and C are plotted in panels (c) and (d), respectively, labeled with the number of graphene monolayers (ML) (after [13]).

spectra for both a hydrogen-treated zerolayer and monolayer sample, contributions from the covalently bound carbon of the $(6\sqrt{3}\times6\sqrt{3})$R30° reconstructed interface layer are completely absent [13, 90]. The only carbon signals observed are related to the SiC bulk and the graphene layer. At annealing temperatures higher than 700 °C the hydrogen starts to desorb, as indicated by the appearance of interface components as found for the pristine $(6\sqrt{3}\times6\sqrt{3})$R30° reconstruction [13].

4. Conclusion and Outlook

In conclusion, we have shown that epitaxial graphene on SiC grows on top of a carbon interface layer that possesses a graphite-like atomic structure. However, due to a strong covalent bonding to the substrate the linear π-bands typical for graphene cannot develop. Only the next carbon layer on top of this interface behaves like monolayer graphene. During the growth of epitaxial graphene on SiC(0001) the number of graphene layers can be precisely controlled by ARPES measurements. The ARPES data were used as a reference to establish LEED fingerprints for a continuous growth control in UHV. Large scale homogeneous graphene samples can be obtained by using a furnace growth technique at higher temperatures [31]. However, due to the influence of the interface layer, epitaxial graphene on SiC(0001) is intrinsically n-doped, regardless of

the growth technique. We have shown that the band structure of epitaxial graphene on SiC(0001) can be precisely tailored by functionalizing the graphene surface with F4-TCNQ molecules. The intrinsic n-doping of the pristine graphene layers can be compensated. Charge neutrality can be achieved for mono- and bilayer graphene. A charge transfer complex is formed by the graphene film and the F4-TCNQ molecular overlayer. The electrons are removed from the graphene layer via the cyano groups of the molecule. In addition, it was found that the molecules remain stable under ambient conditions, at elevated temperatures and can be applied via wet chemistry so that the incorporation of this doping method into existing technological processes appears feasible [42]. In bilayer graphene, the hole doping allows the Fermi level to shift into the energy band gap. The additional dipole developing at the interface with the F4-TCNQ overlayer causes the band gap magnitude to increase to more than double of its original value. The structural and electronic influence of the interface layer can be completely eliminated by decoupling the graphene from the SiC substrate. It was demonstrated that hydrogen can migrate under the interface layer, bind to the Si atoms of the SiC(0001) surface and achieve this decoupling. The hydrogen passivates the underlying SiC substrate similar to the case of bare SiC surfaces. The interface layer alone transforms into a quasi-free standing monolayer. n-layer graphene films transform into (n+1)-layer graphene films (n=0,1,2,3). In combination with atmospheric pressure graphene growth, the intercalation opens up the possibility to produce quasi-free standing epitaxial graphene on large SiC wafers [90]. The intercalated hydrogen is sustained in ambient conditions and stable up to 700 °C. The intercalation process is technologically well adapted and represents a highly promising route towards epitaxial graphene based nanoelectronics.

5. Acknowledgments

The authors would like to thank C.L. Frewin, C. Locke and S.E. Saddow (University of South Florida) for hydrogen etching of the SiC substrates. C.C. acknowledges the Alexander von Humboldt research fellowship for financial support. The research leading to these results has received funding by the European Community - Research Infrastructure Action under the FP6 "Structuring the European Research Area" Programme (through the Integrated Infrastructure Initiative "Integrating Activity on Synchrotron and Free Electron Laser Science") and from the European Community's Seventh Framework Programme (FP7/2007-2013) under grant agreement no. 226716. Support by the staff at MAX-Lab (Lund, Sweden) and SLS (Villigen, Switzerland) is gratefully acknowledged. We are indebted to L. Patthey and A.A. Zakharov for their advice and support during the synchrotron and LEEM measurements.

References

[1] Wallace P R 1947 *Phys. Rev.* **71** 622
[2] Novoselov K S, Geim A K, Morozov S V, Jiang D, Katsnelson M I, Grigorieva I V, Dubonos A A and Firsov A A 2005 *Nature* **438** 197
[3] Zhang Y, Tan Y-W, Stormer H L and Kim P 2005 *Nature* **438** 201
[4] Geim A K and Novoselov K S 2007 *Nature Materials* **6** 183
[5] de Heer W A, Berger C, Wu X, First P N, Conrad E H, Li X, Li T, Sprinkle M, Hass J, Sadowski M L, Potemski M and Martinez G 2007 *Solid State Commun.* **143** 92
[6] Geim A K 2009 *Science* **324** 1530
[7] Novoselov K S, Geim A K, Morozov S V, Jiang D, Zhang Y, Dubonos S V, Grigorieva I V and Firsov A A 2004 *Science* **306** 666
[8] Berger C, Song Z, Li T, Li X, Ogbazghi A Y, Feng R, Dai Z, Marchenkov A N, Conrad E H, First P N, and de Heer W A 2004 *J. Phys. Chem.* B **108** 19912.
[9] Wintterlin J and Bocquet M-L 2009 *Surface Science* **603** 1841
[10] Park S and Ruoff R S 2009 *Nature Nanotechnology* **4** 217
[11] Gomez-Navarro C, Burghard M and Kern K 2008 *Nano Letters* **8**, 2045
[12] Meyer J C, Geim A K, Katsnelson M I, Novoselov K S, Booth T J and Roth S 2007 *Nature* **446** 60-63
[13] Riedl C, Coletti, C, Iwasaki, T, Zakharov A A and Starke U 2009 *Phys. Rev. Lett.* **103** 246804
[14] Peierls R E 1935 *Ann. I. H. Poincaré* **5** 177
[15] Landau L D 1937 *Phys. Z. Sowjetunion* **11** 26
[16] Reich S, Maultzsch J, Thomsen C, Ordejón P 2002 *Phys. Rev.* B **66** 035412
[17] Castro Neto A H, Guinea F, Peres N M R, Novoselov K S, and Geim A K 2009 *Rev. Mod. Phys.* **81** 109
[18] Semenoff G W 1984 *Phys. Rev. Lett.* **53**, 2449 (1984)
[19] Novoselov K S, McCann E, Morozov S V, Fal'ko V I, Katsnelson M I, Zeitler U, Jiang D, Schedin F and Geim A K 2006 *Nat. Phys.* **2** 177
[20] Katsnelson M I, Novoselov K S and Geim A K 2006 *Nat. Phys.* **2** 620
[21] Katsnelson M I and Novoselov K S 2007 *Solid State Commun.* **143** 3
[22] McCann E and Fal'ko V I 2006 *Phys. Rev. Lett.* **96** 086805
[23] Castro E V, Novoselov K S, Morozov S V, Peres N M R, Lopes dos Santos J M B, Nilsson J, Guinea F, Geim A K and Castro Neto A H 2007 *Phys. Rev. Lett.* **99** 216802
[24] Zhang Y, Tang T-T, Girit C, Hao Z, Martin M C, Zettl A, Crommie M F, Shen Y R and Wang F 2009 *Nature* **459** 820
[25] N'Diaye A T, Bleikamp S, Feibelman P J and Michely T 2006 *Phys. Rev. Lett.* **97** 215501
[26] Marchini S, Günther S and Wintterlin J 2007 *Phys. Rev.* B **76** 075429
[27] Sutter P W, Flege J-I and Sutter E A 2008 *Nature Materials* **7** 406
[28] Berger C, Song Z, Li X, Wu X, Brown N, Naud C, Mayou D, Li T, Hass J, Marchenkov A N, Conrad E H, First P N, and de Heer W A 2006 *Science* **312** 1191
[29] Ohta T, Bostwick A, Seyller T, Horn K and Rotenberg E 2006 *Science* **313** 951
[30] Riedl C, Starke U, Bernhardt J, Franke M and Heinz K 2007 *Phys. Rev.* B **76** 245406
[31] Emtsev K V, Bostwick A, Horn K, Jobst J, Kellogg G L, Ley L, McChesney J L, Ohta T, Reshanov S A, Rotenberg E, Schmid A K, Waldmann D, Weber H B and Seyller T 2009 *Nature Materials* **8** 203
[32] Lin Y-M, Dimitrakopoulos C, Jenkins K A, Farmer D B, Chiu H-Y, Grill A, Avouris P 2010 *Science* **327** 662
[33] van Bommel A J, Crombeen J E and van Tooren A 1975 *Surf. Sci.* **48** 463
[34] Forbeaux I, Themlin J-M and Debever J-M 1998 *Phys. Rev.* B **58** 16396
[35] Starke U and Riedl C 2009 *J. Phys.*: CM **21** 134016
[36] Virojanadara C, Syväjarvi M, Yakimova R, Johansson L I, Zakharov A A and Balasubramanian

T 2008 *Phys. Rev. B* **78** 245403
[37] Al-Temimy A, Riedl C and Starke U 2009 *Appl. Phys. Lett.* **95** 231907
[38] Moreau E, Ferrer F J, Vignaud D, Godey S and Wallart X 2010 *Phys. Status Solidi* A **207** 300
[39] Ohta T, Bostwick A, McChesney J L, Seyller T, Horn K, Rotenberg E 2007 *Phys. Rev. Lett.* **98** 206802
[40] Riedl C, Zakharov A A and Starke U 2008 *Appl Phys. Lett.* **93** 033106
[41] Gierz I, Riedl C, Starke U, Ast C R and Kern K 2008 *Nano Letters* **8** 4603
[42] Coletti C, Riedl C, Lee D-S, Krauss B, Klitzing K v, Smet J and Starke U 2010 *Phys. Rev.* B **81** 235401
[43] Soubatch S, Saddow S E, Rao S P, Lee W Y, Konuma M and Starke U 2005 *Mat. Sci. Forum* **483-485** 761
[44] Frewin C L, Coletti C, Riedl C, Starke U and Saddow S E 2009 *Mat. Sci. Forum* **615-617** 589
[45] Tsuchida H, Kamata I and Izumi K 1999 *J. Appl. Phys.* **85** 3569
[46] Seyller T 2004 *J. Phys.*: CM **16** S1755
[47] Coletti C, Frewin C L, Hoff A M and Saddow S E 2008 *Electrochem. Solid-State Lett.* **11** H285
[48] Patthey L, Schmidt T, Flechsig U, Quitmann C, Shi M, Betemps R, Botkine M and Abela R 2002 *in PSI Scientic Report 1999/Volume VII, Surface/Interface Spectroscopy Beamline* (Paul Scherrer Institut)
[49] Nyholm R, Andersen J N, Johansson U, Jensen B N and Lindau I 2001 *Nucl. Instr. and Meth. in Phys. Res.* A **467-468** 520
[50] Starke U, in: Silicon Carbide, Recent Major Advances (eds: Choyke W J, Matsunami H and Pensl G), p. 281-316, Atomic structure of SiC surfaces, (Springer, 2004)
[51] Starke U, Schardt J, Bernhardt J, Franke M, Reuter K, Wedler H, Heinz K, Furthmüller J, Käckell P and Bechstedt F 1998 *Phys. Rev. Lett.* **80** 758
[52] Starke U, Schardt J, Bernhardt J, Franke M and Heinz K 1999 *Phys. Rev. Lett.* **82** 2107
[53] Emtsev K V, Seyller T, Speck F, Ley L, Stojanov P, Riley J D, Leckey R G C 2007 *Mat. Sci. Forum* **556-557** 525
[54] Emtsev K V, Speck F, Seyller T, Ley L and Riley J D 2008 *Phys. Rev.* B **77** 155303
[55] Mårtensson P, Owman F and Johansson L I 1997 *Phys. stat. sol.* (b), **202** 501
[56] Chen W, Xu H, Liu L, Gao X, Qi D, Peng G, Tan S C, Feng Y, Loh K P and Wee A T S 2005 *Surf. Sci.* **596** 176
[57] Simon L, Bischoff J L and Kubler L 1999 *Phys. Rev.* B **60** 11653
[58] Riedl C 2010 *Dissertation* University Erlangen-Nürnberg, to be published on www.opus.ub.uni-erlangen.de
[59] Starke U, Schardt J and Franke M 1997 *Appl. Phys.* A **65** 587
[60] Starke U, Franke M, Bernhardt J, Schardt J, Reuter K and Heinz K 1998 *Mat. Sci. Forum* **264-268** 321
[61] Riedl C, Virojanadara C, and Starke C 2008 *MAX-lab activity report 2007* (eds.: Johansson U, Nyberg A, Nyholm R, and Ullman H), National Laboratory Lund Sweden
[62] Kim S, Ihm J, Choi H J, and Son Y-W 2008 *Phys. Rev. Lett.* **100** 176802
[63] Varchon F, Mallet P, Veuillen J-Y, and Magaud L 2008 *Phys. Rev. B* **77** 235412
[64] Bostwick A, Ohta T, McChesney J L, Emtsev K V, Seyller T, Horn K and Rotenberg E 2007 *New J. Phys.* **9** 385
[65] Note that the precise calibration of the number of layers for this data set was carried out using ARPES as shown below.
[66] A Shirley background was subtracted from the C 1s data and a linear background from the Si 2p data. The C 1s graphene related peak was fitted using a Doniach-Sunjic profile to account for the metallic behavior, all the other fitted lines are an approximation of the Voigt function. For fitting parameters see [58].
[67] Emtsev K V 2009 *Dissertation* University Erlangen-Nürnberg, www.opus.ub.uni-erlangen.de/opus/volltexte/2009/1360

[68] Zhou S Y, Gweon G-H, Fedorov A V, First P N, de Heer W A, Lee D-H, Guinea F, Castro Neto A H and Lanzara A 2007 *Nature Materials* **6** 770
[69] Stolyarova E, Rim K T, Ryu S, Maultzsch J, Kim P, Brus L E, Heinz T F, Hybertsen M S and Flynn G W 2007 *Proc. Natl. Acad. Sci. USA* **104** 9209
[70] Riedl C and Starke U 2009 *Mat. Sci. Forum* **615-617** 219
[71] Hibino H, Kageshima H, Maeda F, Nagase M, Kobayashi Y and Yamaguchi H 2008 *Phys. Rev.* B **77** 075413
[72] Lee D S, Riedl C, Krauss B, v. Klitzing K, Starke U and Smet J H 2008 *Nano Letters* **8** 4320
[73] Ni Z H, Chen W, Fan X F, Kuo J L, Yu T, Wee A T S and Shen Z X 2008 *Phys. Rev.* B **77** 115416
[74] Faugeras C, Nerrière A, Potemski M, Mahmood A, Dujardin E, Berger C and de Heer W A 2008 *Appl. Phys. Lett.* **92** 011914
[75] Röhrl J, Hundhausen M, Emtsev K V, Seyller T, Graupner R and Ley L 2008 *Appl. Phys. Lett.* **92** 201918
[76] Bostwick A, Ohta T, Seyller T, Horn K and Rotenberg E 2007 *Nature Physics* **3** 36
[77] Schedin F, Geim A K, Morozov S V, Hill E W, Balke P, Katsnelson M I and Novoselov K 2007 *Nature Materials* **6** 652
[78] Wehling T O, Novoselov K S, Morozov S V, Vdovin E E, Katsnelson M I, Geim A K and Lichtenstein A I 2008 *Nano Letters* **8** 173
[79] Zhou S Y, Siegel D A, Fedorov A V and Lanzara A 2008 *Phys. Rev. Lett.* **101** 086402
[80] Chen W, Qi D, Gao X and Wee A T S 2009 *Prog. Surf. Sci.* **84** 279
[81] Bekyarova E, Itkis M E, Ramesh P, Berger C, Sprinkle M, de Heer W A and Haddon R C 2009 *J. Am. Chem. Soc.* **131** 1336
[82] Lu Y H, Chen W, Feng Y P and He P M 2009 *J. Phys. Chem.* B **113** 2
[83] Zhou X, Pfeiffer M, Blochwitz J, Werner A, Nollau A, Fritz T and Leo K 2001 *Appl. Phys. Lett.* **78** 410
[84] Wells S K, Giergel J, Land T A, Lindquist J M and Hemminger J C 1991 *Surf. Sci.* **257** 129
[85] Chen W, Chen S, Qui D C, Gao X Y and Wee A T S 2007 *J. Am. Chem. Soc.* **129** 10418
[86] Lindquist J M and Hemminger J C 1998 *J. Phys. Chem.* **92** 1394
[87] Romaner L, Heimel G, Bredas J-L, Gerlach A, Schreiber F, Johnson R L, Zegenhagen J, Duhm S, Koch N and Zojer E 2007 *Phys. Rev. Lett.* **99** 256801
[88] Qi D, Chen W, Gao X, Wang L, Chen S, Loh K P and Wee A T S 2007 *J. Amer. Chem. Soc.* **129** 8084
[89] Riedl C, Coletti, C, Iwasaki, T, Zakharov A A and Starke U 2010 *Mat. Sci. Forum* **645-648** 623
[90] Forti S, Riedl C, Coletti C, Emtsev K V, Zakharov A A and Starke U, unpublished.